Analyst

Accepted Manuscript

This article can be cited before page numbers have been issued, to do this please use: Y. Wang, L. Nan, Y. Jiang, M. Fan, J. Chen, P. Yuan, A. Wang and J. Feng, *Analyst*, 2020, DOI: 10.1039/C9AN02442E.

ROYAL SOCIETY OF CHEMISTRY

rsc.li/analyst

View Article Online
DOI: 10.1039/C9AN02442E

A robust and efficient aqueous electrochemiluminescence emitter constructed by sulfonate porphyrin-based metal-organic framework and its application in ascorbic acid detection

Yi-Wen Wang, Li-Jiao Nan, Yi-Rong Jiang, Miao-Feng Fan, Jun Chen, Pei-Xin Yuan,* Ai-Jun Wang, Jiu-Ju Feng *

Key laboratory of the Ministry of Education for Advanced Catalysis Materials, College of Chemistry and Life Sciences, College of Geography and Environmental Sciences, Zhejiang Normal University, Jinhua 321004, China

**Corresponding author. Email: ypxdr@zjnu.edu.cn (P.X. Yuan); jjfeng@zjnu.cn (J.J. Feng).*

Abstract

Robust and strong electrochemiluminescence (ECL) emission of organic emitters in aqueous solution is crucial for expanding their applications in early diagnosis. Herein, Zn-based porphyrin-based metal-organic-framework ((Zn)porphMOF) was facilely obtained by chelating Zn(II)meso-tetra (4-sulfonatophenyl) porphine (Zn-TSPP) with Zn ion, showing substantially enhanced ECL radiation with $K_2S_2O_8$-coreactants *via* the "reduction-oxidation" route in aqueous media. Contrast with Zn-TSPP, the ECL intensity of the (Zn)porphMOF displayed 22-time increase in the ECL intensity because of the agglomeration effects. By virtue of the dramatic confinement toward the energy and electron transfer of ascorbic acid (AA) during the ECL process, an ultrasensitive biosensor was developed with a wide linear range (3.77 to 26.4 μM) and ultra-low detection limit of 0.29 μM (3 *S/N*). This work offers a feasible avenue to harvest the steady and boosted ECL responses of organic molecular in aqueous media, also greatly expanding the MOF application in bioanalysis.

Keywords: Porphyrin; Metal-organic-framework; Electrochemiluminescence; Emitter; Biosensor.

1. Introduction

Electrochemiluminescence (ECL), usually generated by the electroactive materials oxidized or reduced on the electrode at appropriate potentials, has widespread applications in diagnostics, environmental assay and (bio) analysis.[1-4] Among them, numerous organic molecules such as polycyclic aromatic hydrocarbons,[5] boron fluoride dipyrrole dyes,[6] tris-(bipyridine)ruthenium(II)[7] and porphyrin[8] demonstrate the unique ECL behaviors in aprotic solvents.

Especially, porphyrins complexes display highly stable heterocycle structures, which are commonly used as photosensitizers and optical probes.[9, 10] However, they are difficult to realize the efficient and stable ECL radiation in aqueous media, due to the low solubility and instability of intermediates as well as the narrow potential window.[11] Therefore, it is urgent to explore efficient and stable ECL emitters for harvesting the brighter ECL radiation in such environment.

Substantial efforts have been made in improving the stability of organic emitters with the aid of advanced nanocarriers (e.g. polymeric micelles,[12] liposomal, dendrimers,[13] silica and its derivatives,[14] along with upconversion nanoparticles.[15] The remarkably improved conductivity and enriched active sites of the supported metal nanoclusters would contribute to the stability of the ECL intermediates and the decrease in the excited potential.[16]

Meanwhile, it is another rational strategy to effectively avoid the collision of the organic emitter with proton by adjusting the solution state.[17] Lately, ion liquid[18] and film-forming polymer like tetraoctyl ammonium bromide[19] were introduced into the detection system to enhance the ECL emission *via* creating the oil-in-water emulsion

and assembly onto the functional electrode. Also, the aggregation induced ECL (AIECL), as a novelty and popular method, is feasible for signal amplification, which is derived from the aggregation of metal organic complexes.[20] Unfortunately, the above methods usually involve toxic heavy metals and/or complicated synthesis, which seriously restrict their practical applications.

Inspired by the AIECL model, porphyrin and its derivatives are easily accumulated together in aqueous circumstance because of their metal coordination heterocycle structures.[21] Thus, the accumulation of porphyrin monomers can effectively harvest the stable and brighter ECL signals. Especially, the symmetric substituent groups (e.g. carboxylate and sulfonic groups) in heterocycle of Zn porphyrin can behaved as organic ligands to coordinate metal ion, in turn forming the metal-organic-frameworks (MOFs).[22]

Furthermore, the above MOFs usually chelate with transition metal that is effectively integrated with nitrogen co-doped carbons (M–N–C, where M = Fe, Co, Zn, etc.).[23] Also, the coordinative unsaturated sites of MOFs are essential for the catalysis and photoelectric conversion.[24] More impressively, the porphyrin-based MOFs have the flexible redox states, heterocyclic aggregation and electronic structures, which play the key roles in photoelectric energy transduction and oxygen reduction.[25] For the aggregation-induced optical effect, the porphyrin-derived MOFs show great potential to achieve stable and brighter ECL in aqueous solution with the aid of reductive co-reactants.[26] Additionally, the unique MOFs commonly exhibit enlarged surface area and homogeneous distribution of pyridinic N, which are rational

View Article Online
DOI: 10.1039/C9AN02442E

to promote free diffusion/photoelectric activity of co-reactants from the inner/outside surfaces during the ECL process.[27]

In this work, Zn(II) meso-tetra(4-sulfonatophenyl)porphine (Zn-TSPP) has the symmetric sulfonates structure and distinctive ECL behaviors, which is selected as a linker to coordinate with Zn ion, in turn forming the Zn-TSPP-derived MOFs (defined as (Zn)porphMOF for clarity). The resultant (Zn)porphMOF displayed the brighter ECL irradiation with the assistance of $K_2S_2O_8$ in aqueous buffer. Then, the (Zn)porphMOF ECL biosensor was developed by virtue of ascorbic acid (AA) as a mediator to restrict the electron and energy transfer,[28] as described in Scheme 1.

2. Experimental section

2.1. Synthesis of (Zn)porphMOF

The (Zn)porphMOF was classically synthesized based on the previous work with

major modification.[29] Firstly, 13 mg of Zn-TSPP, 59.5 mg of $Zn(NO_3)_2$ and 21 mg of 1,3,5-benzenetricarboxylic acid (BTC) were all individually dispersed into 1 mL of *N*,*N*-dimethylformamide (DMF) under mild stirring, followed by mixing them together. The mixed solution was then heated up to 90°C and kept static for 48 h. The resulting dark brown precipitates were obtained by centrifugation at 6,000 rpm for 15 min, and thoroughly washed consecutively with ethanol and water to remove unbound substances. The resulting product was re-suspended in water for further use.

2.2. Detection of AA with the ECL platform

Prior to the ECL measurements, a glassy carbon electrode (GCE, 3 mm in diameter) was cleaned sequentially with 0.3 and 0.05 μm aluminum slurry, and then rinsed thoroughly with water to remove the residual alumina powder. Next, the well-polished electrode was dried by high-purity nitrogen (N_2) for further test.

The ECL measurements were carried out by immersing the freshly-cleaned electrode into the phosphate buffer solution (PBS, 0.1 M K_2HPO_4 + 0.1 M KH_2PO_4 + 0.25 M KCl, pH 7.4) containing 0.9 μM (Zn)porphMOF at different AA concentrations, where 20 mM $K_2S_2O_8$ performed as the co-reactant. The electrochemical measurements were conducted in the similar way.

In addition, the ECL measurements and electrochemical tests of blank Zn-TSPP and the other references were all performed under the same conditions if not stated otherwise.

View Article Online
DOI: 10.1039/C9AN02442E

3. Results and discussion

3.1. Morphology and structure characterization

Transmission electron microscopy (TEM) and X-ray photoelectron spectroscopy (XPS) measurements were performed to characterize the morphological and structural features of the typical sample. As shown in Fig. 1A, there emerges many cylinder-like structures with uniformly and vertically orientations as well as smooth surfaces. Also, the lengths of the as-formed nanorods are a few micrometers with well-distributed diameters.

Furthermore, high-magnification TEM image was utilized to check the structures, where uniform cylinder-like structures emerge (Fig. 1B), with smooth boundary and the average diameter in the range of 200~500 nm. Most notably, there is no any lattice fringe detected, certificating the amorphous crystal structures of the sample, thanks to the formation of the C-N orderly accumulation in the synthetic conditions. It can be seen that the (Zn)porphMOF shows the obvious nanorod and large active surface generated by orderly coordination.[30]

The chemical bonds and compositions of advanced nanoparticles can be powerfully illustrated by X-ray photoelectron spectroscopy (XPS).[31-33] As seen in Fig. S1, four binding energies (BEs) at 167.84, 283.96, 399.28, and 1021.81 eV coincide well with S, C, N and Zn elements for the (Zn)porphMOF, respectively.[34] The strong BEs at 1044.91 and 1021.89 eV correspond to Zn^{2+} species,[35] indicating that Zn^{2+} is the major in the product (Fig. 1C, curve a). The XPS peaks (1044.91 and 1021.89 eV) have obvious red shifts alternative to those of pure Zn-TSPP (1043.92 and 1020.91

eV, Fig. 1C, curve b),[36] displaying the strong ability of the Zn-TSPP accumulated into the MOF aggregates.

As clearly illuminated by the N 1s XPS section, both pyrrole N and pyridine N show up in the (Zn)porphMOF (curve a) and Zn-TSPP (curve b) (Fig. 1D). The pyrrole N shows up at 399.40 eV with strong intensity and the weak peak of the pyridine N emerges at 338.34 eV.[37] By comparison, the corresponding N species all display the evident positive shifts for the Zn-TSPP (397.39 and 339.22 eV, curve b).[38] These changes imply the changes in the N states and the enhanced stability of Zn ion *via* orderly coordination of the Zn-TSPP with Zn ion to form (Zn)porphMOF through the Zn-N-C bond.[39-40]

Meanwhile, the S 2p XPS segment was also provided to examine whether the efficient coordination between the Zn-TSPP and Zn ion. As Fig. S2 illustrates, the peak at 168.04 eV is attributed to S element in the (Zn)porphMOF, which displays an obvious red shift relative to that of Zn-TSPP itself (at 167.63 eV), reflecting the efficient formation of the Zn-S bond,[41] as further validated by the Zn 2p XPS spectrum. Especially, the normalized atomic concentration of N1s/Zn 2p is calculated to be roughly 2.66:19.99 based on the XPS peaks, which is close to 3:20, implying that one Zn ion links with two Zn-TSPP monomers. As a result, the (Zn)porphMOF is formed by the coordination of Zn ion with the sulfonic group from Zn-TSPP, albeit with still existence of the Zn-N-C bond in the complexes.

3.2. UV–vis absorbance and fluorescence spectroscopy characterization

View Article Online
DOI: 10.1039/C9AN02442E

UV–vis absorbance and fluorescence spectroscopy measurements were adopted to investigate the optical activity of the as-synthetized (Zn)porphMOF, using Zn-TSPP as the contrary. For Zn-TSPP, an obvious absorbance peak (Sort band) at 422 nm and the Q bands at 558 and 600 nm (Fig. 2A, curve a) correspond to the typical porphyrin ring absorbance and its coordination with Zn ion,[42] respectively. Impressively, similar absorbance peak shows up at 424 nm for the (Zn)porphMOF (Fig. 2A, curve b), while the Q bands disappear with the obviously enhanced baseline, due to the scattering effects of the as-formed nanomaterials.[43] Taken together, these observations demonstrate the efficient synthesis of (Zn)porphMOF without any destroy in the key structure.

Meanwhile, the FL signals of the samples were acquired at the excitation wavelength of 424 nm (Fig. 2B). Specifically, a huge doublet FL peaks emerge at 606 and 658 nm for the Zn-TSPP (curve a), thanks to the photoexcitation of porphyrin heterocycles towards Zn ion.[44] More notably, the peak intensities of the (Zn)porphMOF (curve b) show the 4-time enhancement alternative to those of the Zn-TSPP (curve a) in the same circumstance, thanks to the stable and orderly integration of porphyrin monomer. Also, the ECL plot of the (Zn)porphMOF is further recorded in the $K_2S_2O_8$ system at the potential of -2.0 V with the help of the optical filters. The emission peak is observed at 540 nm (Fig. S3), displaying the obviously red shift with respective to that of the FL spectrum (Fig. 2B, curve a), owing to the different excitation pathways and restricted sensitivity of the instrument. In the contrary experiment, there is not any FL response discovered in the PBS (pH

7.4) only containing 20 mM $K_2S_2O_8$ (curve c). To this end, these phenomena demonstrate the as-prepared (Zn)porphMOF as brighter luminescent emitter.

3.3. The ECL mechanism of the (Zn)porphMOF

With the excellent optical performances of the (Zn)porphMOF, the respective ECL behaviors and ECL mechanism were further studied by ECL and CV synchronously. As Fig. 3A illuminates, there is not any ECL signal detected at bare GCE in the PBS only containing 20 mM $K_2S_2O_8$ (Fig. 3A, curve a). Meanwhile, a sharp reduction peak shows up at -1.54 V on the CV plot (Fig. 3B, curve a), which belongs to the reduction of $S_2O_8^{2-}$ during the process [45]. Alternatively, an obvious ECL peak appears at -1.98 V with the peak intensity of 14800 a.u. in the presence of 0.9 μM (Zn)porphMOF + 20 mM $K_2S_2O_8$ (Fig. 3A, curve b), along with a strong reduction peak emerged at -1.61 V on the correlated CV curve (Fig. 3B, curve b). These observations indicate the highly boosted catalytic property of the (Zn)porphMOF for the reduction of $S_2O_8^{2-}$ in the system.

In another control, there appears a week ECL responses (c.a. 180 a.u.) at -1.98 V in the PBS only containing 0.9 μM (Zn)porphMOF (Fig. 3A, curve c), and a pair of redox peaks shows up at -1.33/-1.22V (Fig. 3B, curve c), corresponding to the transformation of Zn^{2+} to Zn^{+} species.[46] To this regard, the (Zn)porphMOF certifies as the feasible ECL luminophore in the aqueous system.

Then, the controlled experiments were conducted in the air- and N_2-satruated conditions in the presence of $K_2S_2O_8$ to examine the effect of oxygen in the ECL

View Article Online
DOI: 10.1039/C9AN02442E

process for the (Zn)porphMOF. As Fig. 3C describes, the ECL intensity of the (Zn)porphMOF only displays a slight decrease (roughly 16%) in the N_2-saturated conditions (curve b) over that acquired in the air-saturated circumstance (curve a). Besides, the reduction peak at -1.54 V on the CV plot displays negligible change in the air-saturated (Fig. 3D, curve a) and N_2-saturated (Fig. 3D, curve b) solutions.

Most impressively, there are two reduction peaks at -0.81 V and -1.61 V for the (Zn)porphMOF on the CV plot in the air-saturated conditions (Fig. S4), which further confirm the oxygen reduction also occurred in this ECL process at -0.81 V.[47] Therefore, it is rational for the ECL emission by combining the (Zn)porphMOF with $K_2S_2O_8$ *via* the "reduction-oxidation" pathway, in which the present oxygen has slight influences on the ECL emission because of the negative-shifted reduction potential of $K_2S_2O_8$ in this study. Therefore, the ECL mechanism can be briefly described as follows:[48, 49]

$$(Zn^{2+})porphMOF + e^- \rightarrow (Zn^{+})porphMOF \ (-1.33\ V) \quad (1)$$

$$K_2S_2O_8 + e^- \rightarrow SO4^{\cdot-} + SO_4^{2-} \ (-1.61\ V) \quad (2)$$

$$SO4^{\cdot-} + (Zn^{+})porphMOF \rightarrow (Zn^{2+})porphMOF^{*} + SO_4^{2-} \quad (3)$$

$$(Zn^{2+})porphMOF^{*} \rightarrow (Zn^{2+})porphMOF + h\nu\ (\lambda_m = 540\ nm) \quad (4)$$

3.4. The ECL behaviors of the (Zn)porphMOF and feasibility of the as-developed biosensor

Based on the ECL mechanism of the (Zn)porphMOF, the ECL behaviors were examined in the $K_2S_2O_8$ system by employing pure Zn-TSPP as the reference. As shown in Fig. 4A, there appears an ECL peak for the Zn-TSPP (curve a), and a

reduced peak is found at -1.48 V on the related CV plot (Fig. 4B, curve a). Using the (Zn)porphMOF instead of Zn-TSPP, the ECL intensity (14800 a.u.) for the (Zn)porphMOF/$K_2S_2O_8$ (Fig. 4A, curve b) clearly displays the 22-fold enhancement relative to that of Zn-TSPP/$K_2S_2O_8$ system (680 a.u., Fig. 4B, curve a), due to the largely boosted catalytic performance of the (Zn)porphMOF for $K_2S_2O_8$ reduction. It certifies the remarkable enhancement of the (Zn)porphMOF in the ECL signals.

As revealed by the FL experiments (Fig. S5), the FL relative intensities are almost remained constant under the ultraviolet light by extending the detection time up to 20 min, while a distinctive decay detected within 5 min for the Zn-TSPP. These results evidently show the superior stability of the (Zn)porphMOF in this system.[50]

In addition, the presence of 18.9 μM AA causes the distinct decay in the ECL intensity (approximately declined to 71.2% of its initial value) in the (Zn)porphMOF/$K_2S_2O_8$ system (Fig. 4A, curve c) with compared to the contrary (Zn)porphMOF/$K_2S_2O_8$ system (Fig. 4A, curve b). Meanwhile, a prominent quasi-reversible redox emerges at -1.18/-1.37 V on the correlated CV curve in the presence of (Zn)porphMOF + AA (Fig. 4B, curve c), owing to the severe blockage of the electron and energy transfer by AA to the ECL reaction.[51] These scenarios endow the feasible assay of AA in the (Zn)porphMOF/$K_2S_2O_8$ system.

3.5. Optimization of the ECL detection system

To achieve the best analytical performances, the concentrations of the (Zn)porphMOF and $K_2S_2O_8$ were optimized in the controlled experiments. As

displayed in Fig. 5A, the ECL signals increase violently with the enlarged concentrations of (Zn)porphMOF up to 0.9 μM in the $K_2S_2O_8$ system, because of the sufficient interactions between the (Zn)porphMOF and $K_2S_2O_8$. Then, the ECL signals inversely decrease by further increasing the concentration up to 1.2 μM, because the excessive (Zn)porphMOF would severely inhibit the reaction of electro reduction with the catalytic substrates (i.e. $K_2S_2O_8$).[52] Thus, 0.9 μM is chosen as the best for the sequent AA detection.

Besides, we further checked the effects of the $K_2S_2O_8$ concentrations on the ECL intensities. As Fig. 5B displays, the ECL intensities increase sharply by boosting the $K_2S_2O_8$ concentrations from 5 to 20 mM, and then achieve the maximum at 20 mM thanks to the remarkable enhancement in the catalytic reduction of $K_2S_2O_8$ by (Zn)porphMOF. However, the ECL responses are seriously decayed with excess $K_2S_2O_8$ (i.e. 30 mM), owing to the limited electrode surface area and spatial steric effects.[53] In the end, 20 mM $K_2S_2O_8$ is chosen as the optimal concentration in the sequent analysis.

3.6. ECL behaviors of the (Zn)porphMOF towards AA

By combining the (Zn)porphMOF with the $K_2S_2O_8$ system, a novel ECL biosensor was constructed for ultrasensitive detection of AA under the optimal conditions. As exhibited in Fig. 6A, the ECL intensities gradually decrease with the enhanced AA concentrations up to 30.2 μM. Also, the data at any point is detected for at least 3 times to guarantee the steady of the ECL biosensor. Specially, the ECL

intensities show linear relationship with the AA concentrations ranging from 3.77 to 26.4 μM. The linear fitting equation (I = -539c/μM + 15530) is harvested with a correlation coefficient of R^2 = 0.998 (Fig. 6B), where I stands for the ECL responses in the presence of $K_2S_2O_8$, and c represents the AA concentration. Also, the detection limit is down to 0.29 μM at 3 times of signal-to-noise ratio (3S/N). In addition, the analytical data are comparable or even superior to those previously reported (See details in Table S1).

Above all, the stability was further examined by the ECL plots of the current biosensor in 3.77 μM AA solution recorded by consecutively scanning for 400 s in the system. As seen in Fig. 6C, the ECL intensities are almost constant during the long-term test, and the relative standard deviation (RSD) is estimated to be 0.13%, suggesting the highly improved stability in this assay.[54]

To validate the reliability and applicability of the developed method, the possible interfering substances such as hydroquinone (HQ), dopamine (DA), resorcinol (R-80), Fe^{2+}, uric acid (UA), and glucose (Glu) were introduced into the detection system. As Fig. 6D describes, the relative ECL intensities are below 10% for the interfering samples, which are much lower than that of AA under the identical operation conditions, showing the highly boosted selectivity of the (Zn)porphMOF towards the AA target. It means the high precision and acceptable reliability of the as-developed biosensor, which are of great significance to develop speedy and expediently AA detection methods in practice.

View Article Online
DOI: 10.1039/C9AN02442E

3.7. Analysis of real samples

The practicality of the as-developed ECL biosensor was estimated by detecting AA in the serum samples by standard addition method.[55] As shown in Table S2, the recoveries emerge in the range of 96.6 %-102.5 % for the 100-fold diluted serum sample. For that, the ECL biosensor reflects the huge potential applications in clinical diagnosis.

4. Conclusions

In this work, the (Zn)porphMOF was prepared through the coordination of Zn-TSPP (as a linker) with zinc ion, which was utilized as ECL luminescent for the ultrasensitive AA detection in the $K_2S_2O_8$ system *via* the "reduction-oxidation" route. The as-constructed (Zn)porphMOF exhibited negligible impact of dissolved oxygen on the ECL test. Contrast with pure Zn-TSPP, the ECL signals of the (Zn)porphMOF exhibited 22-fold increase under the same circumstance, due to the more stable ECL intermediates and frame aggregation effects. By virtue of AA as the mediator to dramatically restrain the energy and electron transfer of the ECL from the (Zn)porphMOF, a novel ECL biosensor was designed and constructed, showing the wide linear range (3.77 to 26.4 μM), ultralow detection limit (0.29 μM) and high selectivity. Hence, the developed strategy would realize the powerful ECL radiation of advanced porphyrin-like organic emitter in aqueous system, and thereby greatly expands their optical applications in early diagnosis and clinical research.

View Article Online
DOI: 10.1039/C9AN02442E

Acknowledgements

This research was supported by Basic Public Welfare Research Project of Zhejiang Province (No. LGG19B050001 and LGG18E010001), Natural Science Foundation of Zhejiang Province (No. Q19B050016), the Open Research Fund of Key Laboratory of the Ministry of Education for Advanced Catalysis Materials (Zhejiang Normal University), and PhD Fund of ZJNU for Young Teachers (No. zz323205020517002104).

References

1. J. L. Liu, J. Q. Zhang, Z. L. Tang, Y. Zhuo, Y. Q. Chai and R. Yuan, *Chem. Sci.*, 2019, **10**, 4497-4501.

2. W. L. Guo, H. Ding, C. Y. Gu, Y. H. Liu, X. C. Jiang, B. Su and Y. H. Shao, *J. Am. Chem. Soc.*, 2018, **140**, 15904-15915.

3. Z. Y. Liu, W. J. Qi and G. B. Xu, *Chem. Soc. Rev.*, 2015, **44**, 3117-3142.

4. S. L. Liu, Q. H. Zhang, L. Zhang, L. Gu, G. Z. Zou, J. C. Bao and Z. H. Dai, *J. Am. Chem. Soc.*, 2016, **138**, 1154-1157.

5. J. L. Liu, Z. L. Tang, J. Q. Zhang, Y. Q. Chai, Y. Zhuo and R. Yuan, *Anal. Chem.*, 2018, **90**, 5298-5305.

6. M. Hesari, K. N. Swanick, J. S. Lu, R. Whyte, S. N. Wang and Z. F. Ding, *J. Am. Chem. Soc.*, 2015, **137**, 11266-11269.

7. G. H. Zhao, Y. G. Wang, X. J. Li, Q. Yue, X. Dong, B. Du, W. Cao and Q. Wei, *Anal. Chem.*, 2019, **91**, 1989-1996.

8. G. Pu, Z. Yang, Y. Wu, Z. Wang, Y. Deng, Y. Gao, Z. Zhang and X. Lu, *Anal. Chem.*, 2019, **91**, 2319-2328.

9. A. K. Mandal, J. R. Diers, D. M. Niedzwiedzki, G. Hu, R. Liu, E. J. Alexy, J. S. Lindsey, D. F. Bocian and D. Holten, *J. Am. Chem. Soc.*, 2017, **139**, 17547-17564.

10. S. Y. Deng, T. T. Zhang, X. B. Ji, Y. Wan, P. Xin, D. Shan and X. J. Zhang, *Anal. Chem.*, 2015, **87**, 9155-9162.

11. J. E. Dick, A. T. Hilterbrand, A. Boika, J. W. Upton and A. J. Bard, *Proc. Natl. Acad. Sci.*, 2015, **112**, 5303.

12. G. J. Chen, R. Jaskula Sztul, C. R. Esquibel, I. Lou, Q. F. Zheng, A. Dammalapati, A. Harrison, K. W. Eliceiri, W. P. Tang, H. Chen and S. Q. Gong, *Adv. Funct. Mater.*, 2017, **27**, 1604671.

13. T. Kambe, A. Watanabe, T. Imaoka and K. Yamamoto, *Angew. Chem. Int. Ed.*, 2016, **55**, 13151-13154.

14. M. F. Delley, G. Lapadula, F. Núñez Zarur, A. Comas Vives, V. Kalendra, G. Jeschke, D. Baabe, M. D. Walter, A. J. Rossini, A. Lesage, L. Emsley, O. Maury and C. Copéret, *J. Am. Chem. Soc.*, 2017, **139**, 8855-8867.

15. Y. F. Li, Z. H. Di, J. H. Gao, P. Cheng, C. Z. Di, G. Zhang, B. Liu, X. H. Shi, L. D. Sun, L. L. Li and C. H. Yan, *J. Am. Chem. Soc.*, 2017, **139**, 13804-13810.

16. S. V. Kruppa, F. Bäppler, W. Klopper, S. P. Walg, W. R. Thiel, R. Diller and C. Riehn, *Phys. Chem. Chem. Phys.*, 2017, **19**, 22785-22800.

17. G. Pu, D. Zhang, X. Mao, Z. Zhang, H. Wang, X. Ning and X. Lu, *Anal. Chem.*, 2018, **90**, 5272-5279.

18. M. A. Hope, K. J. Griffith, B. Cui, F. Gao, S. E. Dutton, S. S. P. Parkin and C. P. Grey, *J. Am. Chem. Soc.*, 2018, **140**, 16685-16696.

19. C. Ye, X. Zhong, R. Yuan and Y. Q. Chai, *Sens. Actuators B Chem*, 2014, **199**, 101-107.

20. S. Carrara, A. Aliprandi, C. F. Hogan and L. De Cola, *J. Am. Chem. Soc.*, 2017, **139**, 14605-14610.

21. D. Dasler, R. A. Schäfer, M. B. Minameyer, J. F. Hitzenberger, F. Hauke, T. Drewello and A. Hirsch, *J. Am. Chem. Soc.*, 2017, **139**, 11760-11765.

22. P. Ling, C. Qian, J. Yu and F. Gao, *Chem. Commun.*, 2019, **55**, 6385-6388.

23. H. G. T. Ly, G. Fu, A. Kondinski, B. Bueken, D. De Vos and T. N. Parac Vogt, *J. Am. Chem. Soc.*, 2018, **140**, 6325-6335.

24. R. Arukula, A. Thota, K. Boga, R. Narayan, B. Sreedhar and C. R. K. Rao, *J. Appl. Polym. Sci.*, 2018, **135**, 46630.

25. S. H. Wang, L. Shang, L. L. Li, Y. J. Yu, C. W. Chi, K. Wang, J. Zhang, R. Shi, H. Y. Shen, G. I. N. Waterhouse, S. J. Liu, J. Tian, T. R. Zhang and H. Y. Liu, *Adv. Mater.*, 2016, **28**, 8379-8387.

26. G. Y. Zhang, C. Cai, S. Cosnier, H. B. Zeng, X. J. Zhang and D. Shan, *Nanoscale*, 2016, **8**, 11649-11657.

27. W. Dong, H. Chen, F. Xia, W. Yu, J. Song, S. Wu, Z. Deng, Z. Y. Hu, T. Hasan, Y. Li, H. Wang, L. Chen and B. L. Su, *J. Mater. Chem. A*, 2018, **6**, 22790-22797.

28. R. Yin, S. Mao, B. Zhao, Z. Chong, Y. Yang, C. Zhao, D. Zhang, H. Huang, J. Gao, Z. Li, Y. Jiao, C. Li, S. Liu, D. Wu, W. Gu, Y. Yang, G. Xu and H. Wang, *J. Am. Chem. Soc.*, 2013, **135**, 10396-10403.

29. Y. Chen, L. Wojtas, S. Ma, M. J. Zaworotko and Z. Zhang, *Chem. Commun.*, 2017, **53**, 8866-8869.

30. S. B. Li, M. Dharmarwardana, R. P. Welch, C. E. Benjamin, A. M. Shamir, S. O. Nielsen and J. J. Gassensmith, *ACS Appl. Mat. Inter.*, 2018, **10**, 18161-18169.

31. J. J. Duan, X. X. Zheng, H. J. Niu, J. J. Feng, Q. L. Zhang, H. Huang and A. J. Wang, *J. Colloid Interface Sci.*, 2020, **560**, 467-474.

32. Y. Chen, X. X. Zheng, X. Y. Huang, A. J. Wang, Q. L. Zhang, H. Huang and J. J. Feng, *J. Colloid Interface Sci.*, 2020, **559**, 206-214.

33. M. F. Fan, H. M. Wang, L. J. Nan, A. J. Wang, X. Luo, P. X. Yuan and J. J. Feng, *Anal. Chim. Acta*, 2020, **1097**, 78-84.

34. D. J. Ma, Q. L. Zhu, X. T. Li, H. C. Gao, X. F. Wang, X. W. Kang and Y. Tian, *ACS Appl. Mat. Inter.*, 2019, **11**, 8009-8017.

35. P. K. Narayanam, V. D. Botcha, M. Ghosh and S. S. Major, *Nanotechnology*, 2019, **30**, 485601.

36. Y. Zhou, Y. Shi, F. Wang and X. Xia, *Anal. Chem.*, 2019, **91**, 2759-2767.

37. H. Cheng, X. Zhou, A. Gao, F. Yi, D. Shu, X. Song, R. Zeng, C. He, S. Li and D. Zeng, *Electrochim. Acta*, 2018, **292**, 20-30.

38. M. Ferrándiz-Saperas, A. Ghisolfi, D. Cazorla-Amorós, C. Nájera and J. M. Sansano, *Chem. Commun.*, 2019, **55**, 7462-7465.

39. L. Osmieri, R. Escudero-Cid, M. Armandi, P. Ocón, A. H. A. Monteverde Videla and S. Specchia, *Electrochim. Acta*, 2018, **266**, 220-232.

40. Y. Xia, G. Wei, X. Liang, J. Zhu, H. Xian, X. Su, H. He and R. Zhu, *J Phys Chem C*, 2019, **123**, 2828-2836.

41. N. R. Shanmugam, S. Muthukumar and S. Prasad, *Anal. Methods*, 2017, **9**, 5525-5533.

42. D. Yim, J. Sung, S. Kim, J. Oh, H. Yoon, Y. M. Sung, D. Kim and W. D. Jang, *J. Am. Chem. Soc.*, 2017, **139**, 993-1002.

43. J. I. Tracey and D. M. O'Carroll, *Adv. Funct. Mater.*, 2018, **28**, 1802630.

44. D. A. Heredia, S. R. Martínez, A. M. Durantini, M. E. Pérez, M. I. Mangione, J. E. Durantini, M. A. Gervaldo, L. A. Otero and E. N. Durantini, *ACS Appl. Mat. Inter.*, 2019, **11**, 27574-27587.

45. E. Han, L. Ding, H. Z. Lian and H. X. Ju, *Chem. Commun.*, 2010, **46**, 5446-5448.

46. P. M. Usov, A. N. Simonov, A. M. Bond, M. J. Murphy and D. M. D'Alessandro, *Anal. Chem.*, 2017, **89**, 10181-10187.

47. Y. H. Wang, J. Wei, P. Radjenovic, Z. Q. Tian and J. F. Li, *Anal. Chem.*, 2019, **91**, 1675-1685.

48. X. Z. Song, X. J. Li, D. Wei, R. Feng, T. Yan, Y. G. Wang, X. Ren, B. Du, H. M. Ma and Q. Wei, *Biosens. Bioelectron.*, 2019, **126**, 222-229.

49. X. Li, Y. Wang, L. Shi, H. Ma, Y. Zhang, B. Du, D. Wu and Q. Wei, *Biosens. Bioelectron.*, 2017, **96**, 113-120.

50. C. C. Wang, H. M. Wang, M. F. Fan, L. Fei, X. Luo, J. J. Feng, P. X. Yuan and A. J. Wang, *Sens. Actuators B Chem*, 2019, **290**, 203-209.

51. H. M. Wang, C. C. Wang, A. J. Wang, L. Zhang, X. Luo, P. X. Yuan and J. J. Feng, *Sens. Actuators B Chem*, 2019, **281**, 588-594.

52. X. J. Li, S. Q. Yu, T. Yan, Y. Zhang, B. Du, D. Wu and Q. Wei, *Biosens. Bioelectron.*, 2017, **89**, 1020-1025.

53. L. Lian, B. Yao, S. Hou, J. Fang, S. Yan and W. Song, *Environ. Sci. Technol.*, 2017, **51**, 2954-2962.

54. M. Zhao, A. Y. Chen, D. Huang, Y. Zhuo, Y. Q. Chai and R. Yuan, *Anal. Chem.*, 2016, **88**, 11527-11532.

55. X. Jiang, H. Wang, H. Wang, Y. Zhuo, R. Yuan and Y. Chai, *Anal. Chem.*, 2017, **89**, 4280-4286.

View Article Online
DOI: 10.1039/C9AN02442E

View Article Online
DOI: 10.1039/C9AN02442E

Fig. 1

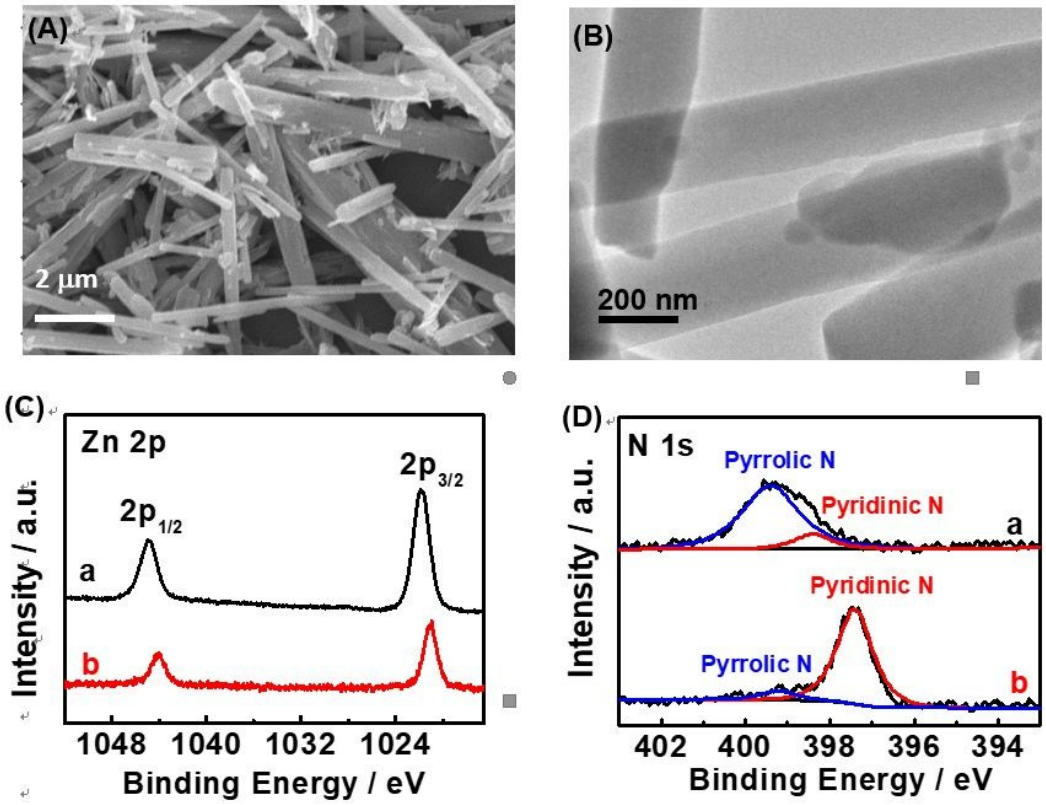

Fig. 1. Typical SEM (A) and high-magnification TEM (B) images of (Zn)porphMOF. The high-resolution Zn 2p (C) and N 1s (D) XPS spectra of (Zn)porphMOF (curve a) and Zn-TSPP (curve b).

Fig. 2

View Article Online
DOI: 10.1039/C9AN02442E

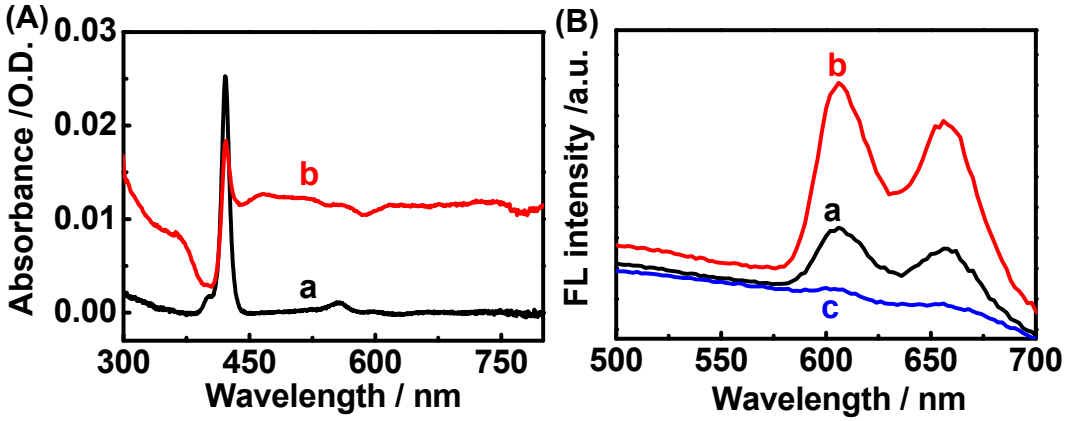

Fig. 2. (A) The UV-vis absorbance spectra of Zn-TSPP (curve a) and (Zn)porphMOF (curve b). (B) The FL emission spectra of Zn-TSPP (curve a), (Zn)porphMOF (curve b) and $K_2S_2O_8$ (curve c) in the PBS (pH 7.4).

Fig. 3

View Article Online
DOI: 10.1039/C9AN02442E

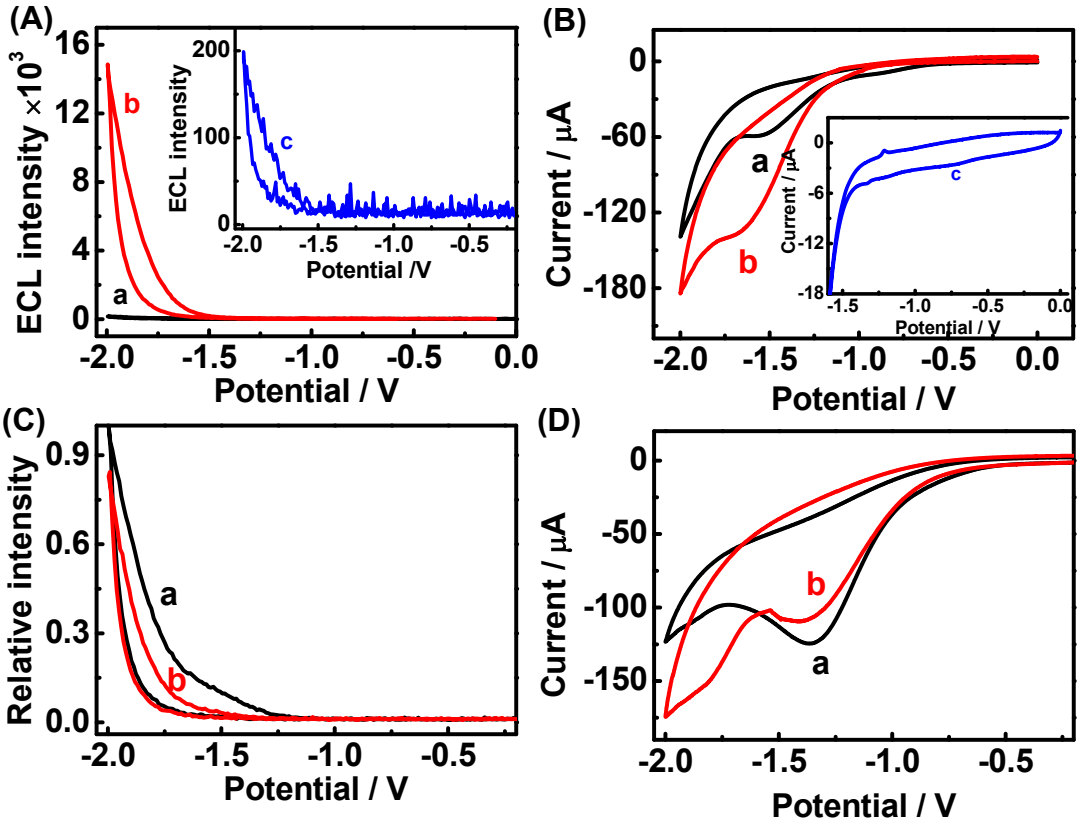

Fig. 3. (A) The ECL and (B) CV plots of bare GCE of 20 mM $K_2S_2O_8$ in PBS (curve a), and the PBS containing (Zn)porphMOF + 20 mM $K_2S_2O_8$ (curve b). Insets in A and B are the ECL and CV curves in the PBS only containing (Zn)porphMOF (curve c). (C) The ECL and (D) CV plots of (Zn)porphMOF in air- (curve a) and N_2-saturated (curve b) PBS containing 20 mM $K_2S_2O_8$.

Fig. 4

View Article Online
DOI: 10.1039/C9AN02442E

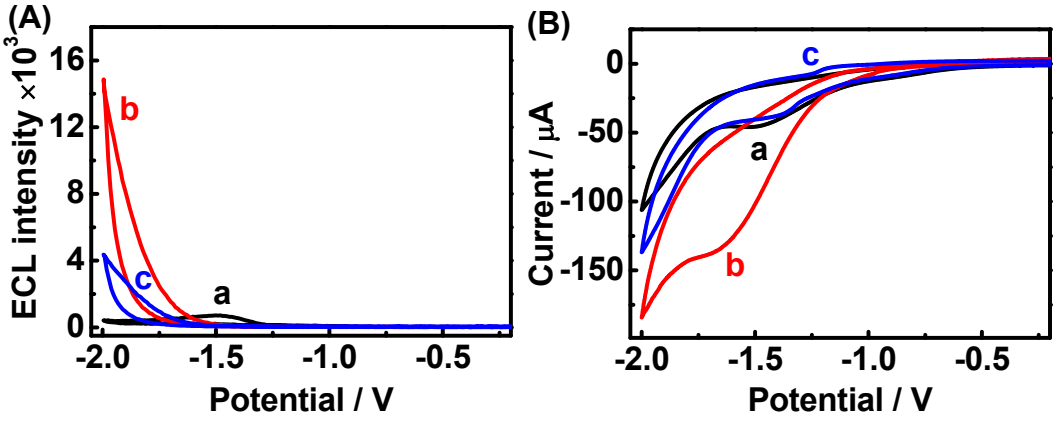

Fig. 4. (A) The ECL signals and (B) CV plots of Zn-TSPP (curve a), (Zn)porphMOF (curve b) and (Zn)porphMOF + AA (curve c) in the PBS containing 20 mM $K_2S_2O_8$.

Fig. 5

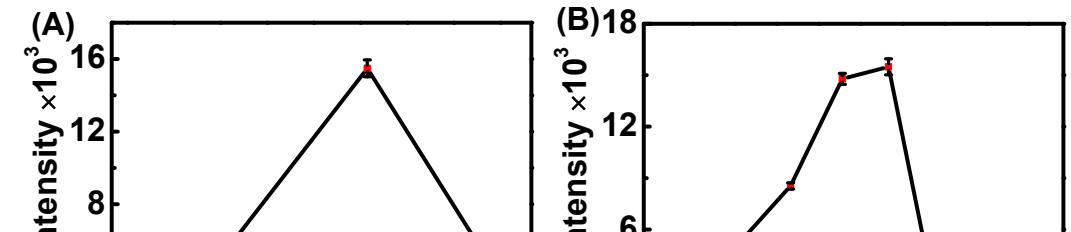

View Article Online
DOI: 10.1039/C9AN02442E

Fig. 5. The ECL responses towards the different amounts of (A) (Zn)porphMOF and (B) $K_2S_2O_8$ in the PBS.

Fig. 6

View Article Online
DOI: 10.1039/C9AN02442E

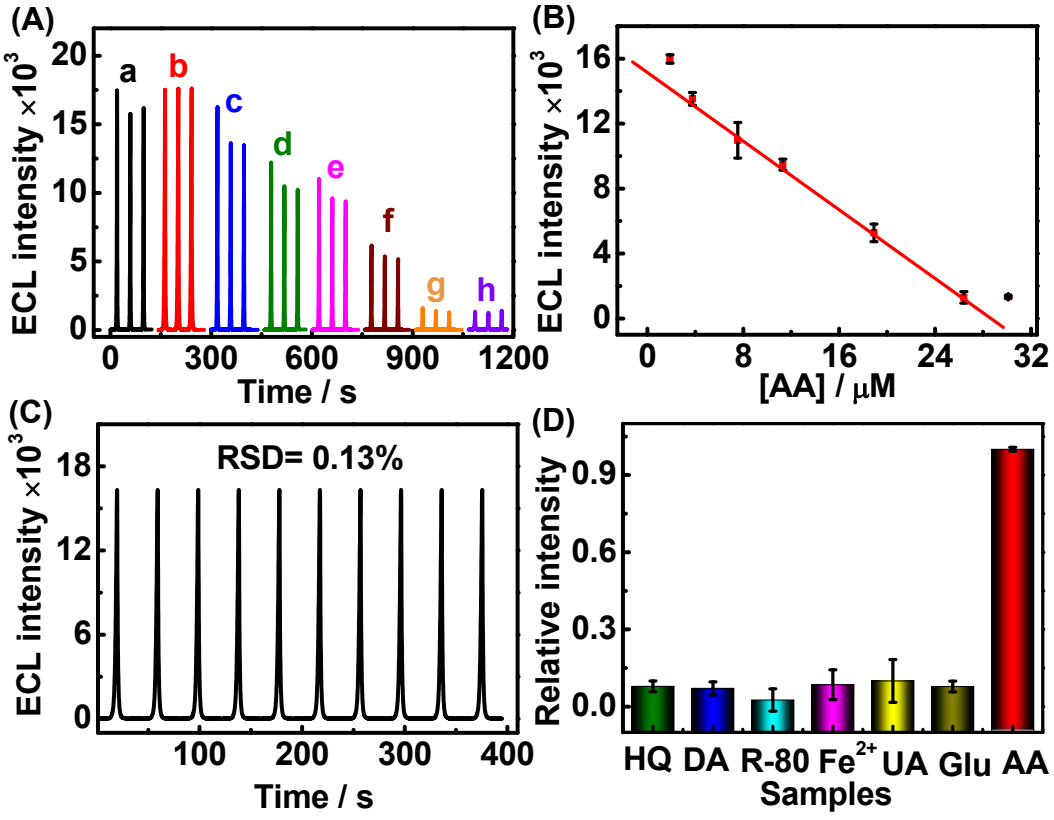

Fig. 6. (A) The ECL responses by boosting the AA concentrations up to 30.2 μM (curves a-h). (B) The calibration curve between the ECL intensities and the AA concentrations. (C) The ECL plots by consecutively scanning for 400 s in the system. (D) The relative intensities towards different interferences.

View Article Online
DOI: 10.1039/C9AN02442E

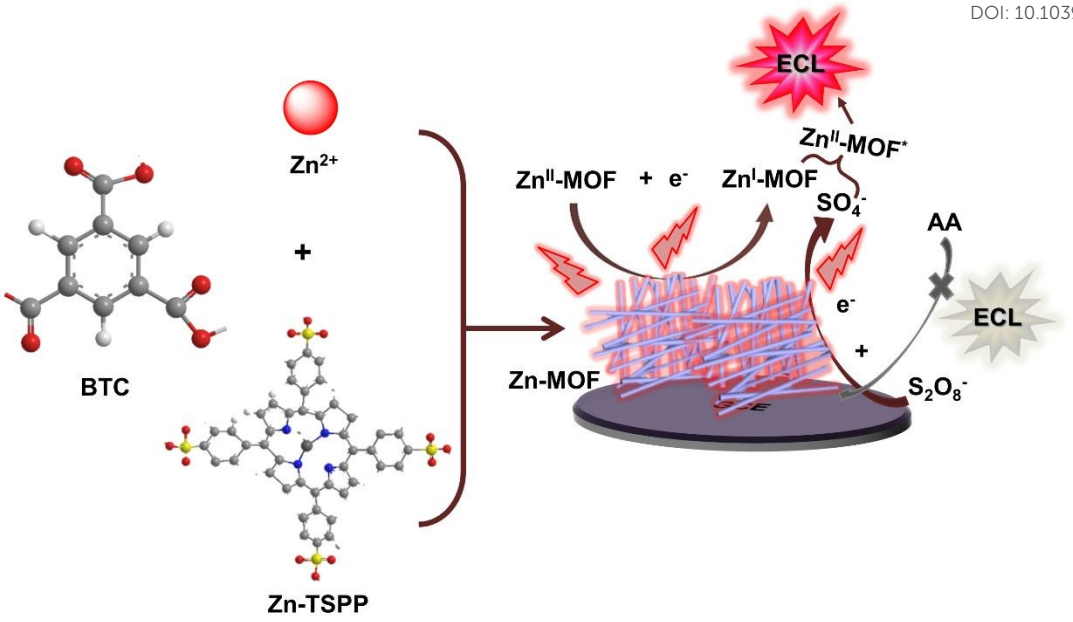

Scheme 1. The scheme of the (Zn)porphMOF based ECL biosensor for AA detection.